Nanoscale

PAPER

View Article Online
View Journal | View Issue

Cite this: *Nanoscale*, 2025, **17**, 2841

Enhancing CO oxidation performance by controlling the interconnected pore structure in porous three-way catalyst particles†

Duhaul Biqal Kautsar,[a] Phong Hoai Le,[a] Ai Ando,[a] Eishi Tanabe,[b] Kiet Le Anh Cao,[a] Eka Lutfi Septiani,[a] Tomoyuki Hirano[a] and Takashi Ogi *[a]

Highly ordered porous structured particles comprising three-way catalyst (TWC) nanoparticles have attracted attention because of their remarkable catalytic performance. However, the conditions for controlling their pore arrangement to form interconnected pore structures remain unclear. In particular, the correlation between framework thickness (distance between pores) or macroporosity and the diffusion of gaseous reactants to achieve a high catalytic performance has not been extensively discussed. Here, the interconnected pore structure was successfully controlled by adjusting the precursor components (*i.e.*, template particle concentration) *via* a template-assisted spray process. A cross-sectional image analysis was conducted to comprehensively examine the internal structure and porous properties (framework thickness and macroporosity) of the porous TWC particles. In addition, we propose mathematical equations to predict the framework thickness and macroporosity, as well as determine the critical conditions that caused the formation of interconnected pores and broken structures in the porous TWC particles. The evaluation of CO oxidation performance revealed that porous TWC particles with an interconnected pore structure, thin framework, and high macroporosity exhibited a high catalytic performance owing to the effective diffusion and utilization of their internal parts. The study findings provide valuable insights into the design of porous TWC particles with interconnected pore structures to enhance exhaust gas emission control in real-world applications.

Received 14th September 2024,
Accepted 23rd December 2024

DOI: 10.1039/d4nr03770g

rsc.li/nanoscale

Introduction

Air pollution is a critical, global environmental and public health challenge primarily aggravated by the widespread use of internal combustion engines. The combustion process generates several toxic compounds, including CO, NO_x, hydrocarbons, and particulate matter, which degrade air quality.[1–4] Various technologies and regulatory measures have been developed to mitigate these emissions. Among them, three-way catalyst nanoparticles (TWC NPs) integrated into catalytic converters play important roles in converting toxic compounds into less harmful substances, such as CO_2, N_2, and H_2O.[5–8] Despite their effectiveness, TWCs present several limitations. Precious metals, such as Pt, Pd, and Rh, used in TWCs, are expensive and limited in supply.[9–12] Another challenge is the strict emission regulations that require catalytic converters to exhibit higher efficiency in the reduction of pollutants.[13,14] A crucial factor in overcoming these challenges is enhancing the catalytic performance through the effective diffusion of reactants to the active sites of TWCs. An improvement in the catalytic performance can enhance the utilization of active sites, which can reduce the need for expensive precious metals and ensure compliance with emission standards.[15–18] Thus, to enhance the catalytic performance of TWCs, catalysts with effective diffusion are required.

Nanostructuring aggregate TWC NPs into porous structures, known as porous TWC particles, is an innovative engineering design for enhancing catalytic performance because it can promote the development of a remarkable interconnected pore structure. The interconnected pore structure is a type of pore

[a]*Chemical Engineering Program, Department of Advanced Science and Engineering, Graduate School of Advanced Science and Engineering, Hiroshima University, 1-4-1 Kagamiyama, Higashi Hiroshima, Hiroshima 739-8527, Japan. E-mail: ogit@hiroshima-u.ac.jp*
[b]*Hiroshima Prefectural Institute of Industrial Science and Technology, 3-10-31 Kagamiyama, Higashi Hiroshima, Hiroshima 739-0046, Japan*

†Electronic supplementary information (ESI) available: Surface pore and particle-size distribution, surface pore density, framework thickness and macroporosity, the critical condition for interconnected pore structure formation, the critical condition for broken structure formation, the mechanism of interconnected pore structure formation in porous TWC particles and the physical properties of porous TWC particles. See DOI: https://doi.org/10.1039/d4nr03770g

arrangement that forms a continuous network by connecting surface and internal pores, thereby facilitating the penetration of reactants from the surface to the internal parts of catalysts.[19–28] Studies have indicated that porous TWC particles synthesized through the polymer template-assisted spray method exhibit higher mass transfer coefficients owing to the effective diffusion of gaseous reactants facilitated by the interconnected pore structure.[14,29] Other studies have shown that porous TWC particles with interconnected pore structures can significantly enhance CO oxidation performance by facilitating high intraparticle convective diffusion within macropores.[13,30] According to the aforementioned studies, the effective diffusion of reactants facilitated by an interconnected pore structure in porous TWC particles is important for increasing the catalytic performance of the particles. In addition, a thin framework and high macroporosity are crucial for enhancing the molecular and convective diffusion of gaseous reactants in porous TWC particles.[13,14,31–33] However, in previous studies, the conditions for precisely controlling the formation of interconnected pore structures were unclear. Furthermore, the correlation among the framework thickness, macroporosity, and catalytic performance of porous TWC particles has not been extensively discussed. These factors are essential for achieving a high catalytic performance in porous TWC particles, which improves adherence to stringent emission standards and reduces costs by decreasing the required amount of catalyst.

Here, the formation of interconnected pore structures was carefully investigated *via* a template-assisted spray process by varying the concentration of a poly(methyl methacrylate) (PMMA) template. The obtained porous TWC particles were examined through focused ion beam (FIB) cross-sectional analysis to confirm their interconnected pore structure and determine the porous properties of the TWC particles, including framework thickness and macroporosity. Furthermore, the porous properties of the synthesized particles were predicted through experimental findings and theoretical modeling. In addition, we propose mathematical equations for determining the critical conditions for the formation of interconnected pores and broken structures of porous TWC particles. CO oxidation was selected as a test reaction to investigate the catalytic performance of the particles. The results showed that the CO oxidation performance increased because of the development of an interconnected pore structure, a thin framework, and the high macroporosity of the porous TWC particles. The study findings provide strategies for designing porous TWC particles with interconnected pore structures, which can enhance the diffusion of gaseous reactants to improve catalytic performance.

Experimental section

Catalyst preparation

The TWC NPs used in this study were provided by Mitsui Mining & Smelting Co., Ltd, Japan. Detailed information about TWC NPs is provided in section 1 of the ESI.† The precursors were prepared by mixing TWC NPs with 0.36 μm-sized PMMA particles (M_w: 100 000 g mol^{-1}, Nippon Shokubai, Japan). The concentration of the TWC NPs was kept constant at 1 wt%, while the concentration of PMMA was varied at 0.1, 0.5, 1, 2, and 3 wt%. The particles obtained from these conditions were named TP0.1, TP0.5, TP1, TP2, and TP3 samples, respectively. The TWC NPs and PMMA particles had positive zeta potentials of +53.3 and +40.6 mV, respectively. Ultrapure water was used as the dispersing medium, and the precursor was mechanically mixed at room temperature through magnetic stirring for 15 minutes followed by ultrasonication for another 15 minutes to ensure uniform particle dispersion. The precursors were fed into a spray drying apparatus comprising an ultrasonic nebulizer, a tubular furnace, a bag filter, and a water trap (Fig. 1a). The tubular furnace was segmented into four zones with temperatures of 250 °C, 350 °C, 500 °C, and 500 °C, while the bag filter was maintained at 150 °C. The droplets generated from the nebulizer were transported to the furnace by an inert carrier gas (N_2) at 0.1 MPa and 5 L min^{-1}. The remaining PMMA from the spray drying process was removed by heating at 900 °C at an increasing temperature rate of 5 °C min^{-1} in air and a gas flow rate of 1 L min^{-1} for 1 h (Fig. 1b).

Characterization

The zeta potentials of the TWC NPs and PMMA particles were measured using a dynamic light scattering instrument (Zetasizer Nano ZSP, Malvern Instruments Ltd, Malvern, UK). Field-emission scanning electron microscopy (FE-SEM; S-5200, 1–5 kV, Hitachi Corp., Japan) was performed to examine the particle morphologies. Using the ImageJ program, the diameter of approximately 300 particles was measured to determine the average size of the particles from the SEM images. In addition, the images were used to determine the surface pore density of the obtained porous TWC particles. Transmission electron microscopy (TEM; JEM-2010, 200 kV, JEOL Corp., Japan) was conducted to observe the inner structure of the particles. FEI Helios PFIB Dual Beam plasma-FIB (PFIB)-SEM equipment was used to obtain cross-sectional SEM images of the samples through an Xe^+ PFIB system. The cross-sectional SEM images were used to measure the framework thickness of the porous TWC particles. Furthermore, the images were used to determine the macroporosity of the particles using the Otsu thresholding technique with ImageJ software.[34,35] X-ray diffraction (XRD; D2 PHASER, Bruker Corp., Billerica, MA, USA) was employed to examine the crystal structure of the samples. N_2 adsorption–desorption isotherms, measured at 77 K using BELSORP-max (Microtract BEL, Japan) according to the Brunauer–Emmett–Teller and Barrett–Joyner–Halenda methods, were used to study the specific surface area (SSA) and pore properties of the particles. The samples were outgassed under vacuum for 6 h at 110 °C to eliminate moisture and other volatile substances prior to the N_2 adsorption–desorption isotherm analysis.

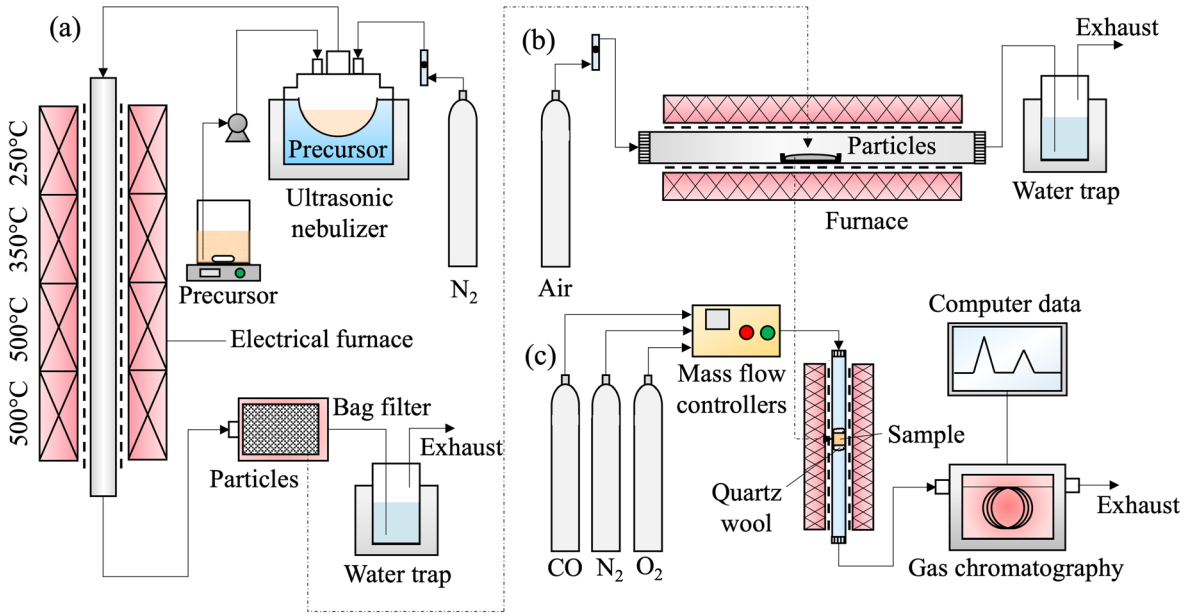

Fig. 1 Experimental setup of (a) the spray drying process, (b) furnace, and (c) catalytic evaluation by gas chromatography.

Catalytic performance evaluation

To evaluate the CO oxidation performance, the porous TWC particles (15 mg) were placed in a quartz tube (inner diameter = 3.8 mm). To ensure stable packing, two layers of quartz wool were placed above and below the sample (Fig. 1c). The first pretreatment involved the introduction of H_2/Ar (5.0 vol%/95.0 vol%), and the second pretreatment was conducted by introducing $CO/O_2/N_2$ (0.80 vol%/0.80 vol%/98.40 vol%). Each pretreatment was conducted at a gas flow rate of 100 mL min^{-1} for 30 min at 200 °C. A gas chromatograph (GC-14B, Shimadzu, Japan) was used to evaluate the catalytic performance. The same mixture and gas flow rate used in the second pretreatment were applied, with the furnace temperature set to the range of 50 °C–300 °C. Eqn (1) was used to calculate the CO conversion to CO_2:

$$\text{CO conversion to CO}_2\,[\%] = \frac{\text{CO}_{\text{in}} - \text{CO}_{\text{out}}}{\text{CO}_{\text{in}}} \times 100\%, \qquad (1)$$

where CO_{in} and CO_{out} represent the peak areas of CO molecules (mol) at the inlet and outlet of the catalyst bed, respectively.

Results and discussion

Fig. 2 shows the morphology of the porous TWC particles when PMMA was used as a template at different concentrations in the precursor. At PMMA concentrations of 0.1–2 wt%, while maintaining the TWC concentration at 1 wt%, spherical porous TWC particles with large open pores on the particle surface were obtained after removing the template (Fig. 2a–d). However, at a PMMA concentration of 3 wt%, certain porous TWC particles were observed to have broken in the TP3 sample (Fig. 2e). This indicated that spherical particles were obtained when the mass ratio of PMMA to TWC was up to 2. A deviation from this ratio can result in non-spherical and fragmented particles. Moreover, increasing the PMMA concentration from 0.1 to 2 wt% led to an increase in the volume of the porous TWC particles, indicated by an increase in their mean geometric diameter from 0.66 to 1.29 μm, respectively (Fig. S5†). In addition, owing to the use of PMMA particles with a uniform size of 0.36 μm, the surface pores had similar sizes with an average diameter of 0.30 μm (Fig. S6†). This slight reduction in pore size can be attributed to particle shrinkage, which occurred as a result of exposure to high temperatures during the synthesis process.[13,14,29,30,36] However, after the spray and template removal process, no sintering was observed within the porous TWC frameworks in all samples, indicating the stability of the porous TWC particles and their active components. These stability characteristics are primarily maintained by the support materials, $CeZrO_4$ and Al_2O_3, present in the TWC particles. Detailed information regarding the stability analysis of porous TWC particles during the synthesis process is provided in section 2 of the ESI.† The SEM images showed that the number of pores increased with an increase in the PMMA concentration, indicating that the number of pores can be controlled by adjusting the PMMA concentration. Fig. 2f shows that the experimental surface pore density (number of pores on the surface of a porous TWC particle divided by its surface area) increased from 0.67 to 3.31 pore per μm^2 with an increase in the PMMA concentration from 0.1 to 2 wt%, respectively. Detailed information regarding the experimental surface pore density is provided in section 4 of the ESI.† To verify the potential for internal pore formation in porous TWC particles, the theoretical surface pore density was calculated. Detailed calculations regarding the theoretical

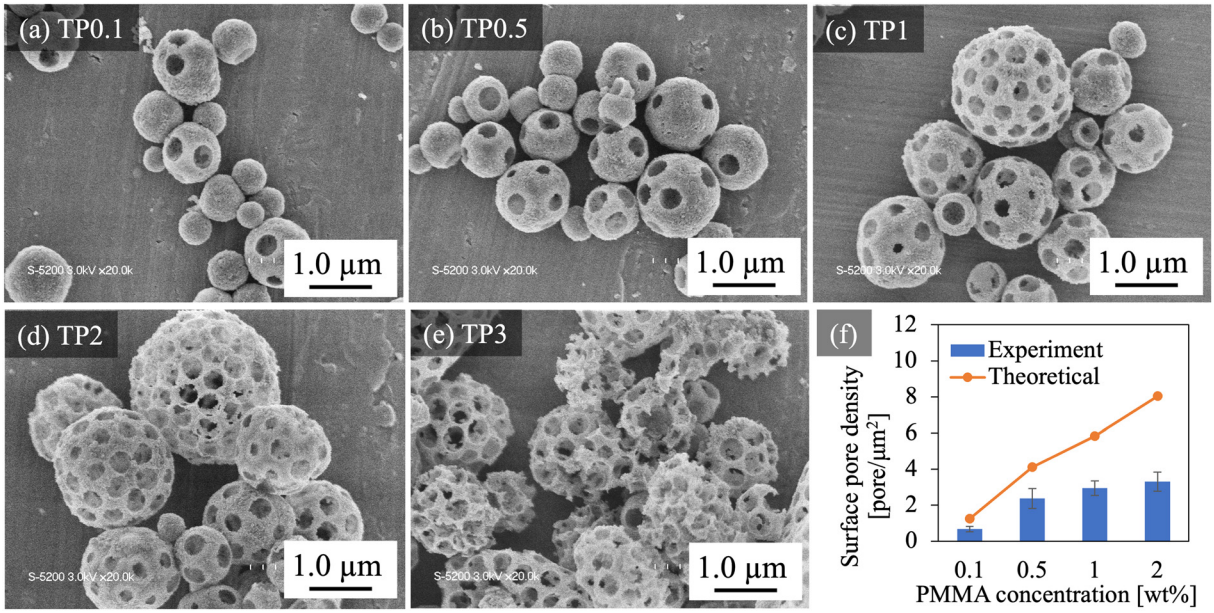

Fig. 2 SEM images of porous TWC particles at PMMA concentrations of (a) 0.1, (b) 0.5, (c) 1, (d) 2, and (e) 3 wt%. (f) Surface pore density at various PMMA concentrations.

surface pore density are available in section 4 of the ESI.† As the result, a similar trend was observed in the calculated curve, where the theoretical surface pore density increased from 1.25 to 4.10 pores per μm^2 at PMMA concentrations of 0.1–0.5 wt%, closely matching the measured values (Fig. 2f). Furthermore, with an increase in the PMMA concentration to 1 and 2 wt%, the differences between the experimental and theoretical surface pore density widened. Although the concentration shifted from 0.5 to 1 and 2 wt%, there was no substantial improvement in the experimental surface pore density, indicating that at both concentrations, the porous TWC particles may possess both surface and internal pores. The internal pores could not be measured from the SEM images, leading to discrepancies between the experimental and calculated results. Thus, further analysis was required to observe the internal parts of the porous TWC particles.

TEM was conducted to observe the internal structure of the TWC particles (Fig. 3). The TEM images showed that without

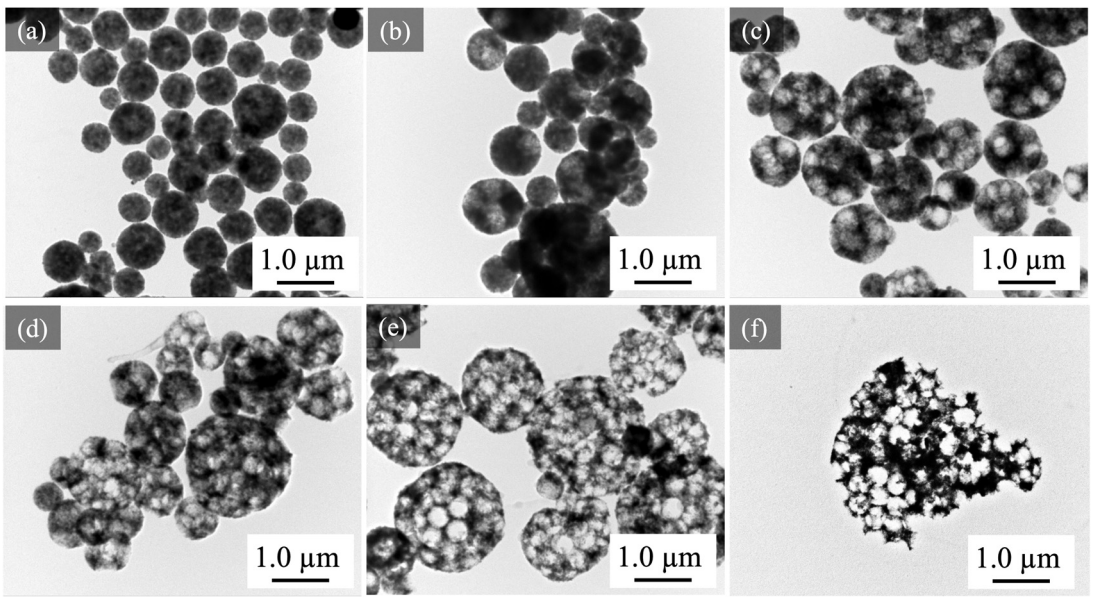

Fig. 3 TEM images of (a) aggregate TWC particles at a concentration of 1 wt% without PMMA and porous TWC particles at PMMA concentrations of (b) 0.1, (c) 0.5, (d) 1, (e) 2, and (f) 3 wt%.

PMMA, no pores were observed in the aggregate TWC particles (Fig. 3a). When PMMA was introduced at concentrations ranging from 0.1 to 2 wt%, certain pores formed in the samples (Fig. 3b–e). Consistent with the SEM images, the number of pores in the porous TWC particles increased with an increase in the PMMA concentration, confirming the controllable pore formation in these particles. Furthermore, the TEM images showed that the TP1 and TP2 particles were more porous than the TP0.5 particles, although the SEM images indicated that these samples had similar experimental surface pore densities. This confirmed the formation of internal pores in porous TWC particles at PMMA concentrations of 1 and 2 wt%. In addition, the broken framework structure of TP3 particles was evident in the TEM analysis when a PMMA concentration of 3 wt% was used in the precursor (Fig. 3f). This broken structure was undesirable and was not investigated further.

Further analysis using FIB cross-sectional SEM images was conducted to observe the internal structure of the porous TWC particles. Fig. 4a shows cross-sectional images captured using the FIB-SEM imaging method. Twelve images of particle slices, taken every 50 nm in depth, were used to comprehensively observe the interconnected pore structure formation in the porous TWC particles. This enabled a deeper understanding of the surface and internal pore distribution in the porous TWC particles at different PMMA concentrations. Fig. S7a† shows the highlighted regions of surface and internal pores in the cross-sectional image of the porous particles. TP0.5, TP1, and TP2 were selected as representative samples. According to Fig. 4b1–12, the TP0.5 particles only exhibited several connected pores located at the periphery of the particles, known as surface pores. This corresponded with the experimental surface pore density, which was similar to the theoretical value at a PMMA concentration of 0.5 wt%, indicating that no internal pores were generated. Furthermore, the TP1 particles only possessed several surface pores at a slice depth in the range of 250–350 nm (Fig. 4c1–3). However, in deeper slices, it was confirmed that a pore was located in the middle of the particles. This pore was categorized as an internal pore because it was located at a slice depth between 400 nm and the middle of the porous TWC particles (Fig. 4c4). At a slice depth in the range of 550–700 nm, all the surface and internal pores were connected, forming an interconnected pore structure (Fig. 4c7–10). This suggested that internal pores play crucial roles in forming interconnected pore networks. Moreover, TP2 began to exhibit an interconnected pore structure from the beginning to the end of the slice depth (Fig. 4d1–12). This demonstrated that at this concentration, the porous TWC particles had a more extensive interconnected pore structure compared with those formed with a PMMA concentration of 1 wt%. At higher PMMA concentrations, there were more areas where pores could form, increasing the pore regions that created interconnected pores throughout the porous TWC particles. Thus, the interconnected pore regions in TP2 became more extensive than those in TP1.

The porous properties (framework thickness and macroporosity) were determined from the FIB cross-sectional SEM images and compared with theoretical calculations. Detailed information regarding the measurements and calculations of the framework thickness and macroporosity is available in section 5 of the ESI.† Fig. 4e shows that the thickness of the particle framework decreased with an increase in the PMMA concentration. Among the three samples, the TP2 sample exhibited the thinnest framework (75.1 nm). The particle framework thickness observed in the experiment was higher than that calculated in all cases. The rearrangement of TWC NPs from the interconnected pore area to other spaces led to the formation of a thicker framework in the real porous TWC particles. However, a similar trend of a decrease in the framework thickness with an increase in the PMMA concentration was observed in the curve. This phenomenon suggested that controlling the formation of the interconnected pore structure by varying the PMMA concentration affected the framework thickness, which can be predicted through calculations. Here, the macroporosity of the porous TWC particles refers to the porosity resulting from the formation of macropores due to the decomposition of PMMA particles. Fig. 4f shows that the macroporosity of the porous TWC particles was directly proportional to the PMMA concentration. The decomposition of PMMA particles produced macropores, which created voids in the particles. Higher PMMA concentrations led to the formation of larger voids, thereby increasing the macroporosity. When the PMMA concentration was increased from 0.5 to 2 wt%, porous TWC particles with macroporosities ranging from 39% to 76.5% were obtained. In addition, the macroporosities obtained from the calculations consistently exceeded the experimental results. The shrinkage of the TWC particles after the reheating process may have reduced the macroporosity of the particles, resulting in a lower macroporosity than that predicted by the calculations. However, a similar trend of an increase in macroporosity with an increase in the PMMA concentration suggested that the change in this property could be predicted by calculations.

As previously mentioned, the interconnected pore structure begins to generate when all the surface and internal pores of the porous TWC particles are connected. According to the morphological analysis, at low PMMA concentrations of 0.1 and 0.5 wt%, pores were only observed on the surface of the porous TWC particles. At these concentrations, the low number of PMMA particles allowed the porous TWC particle surface area to accommodate all the PMMA particles on the surface. Under these conditions, interconnected pore formation was not observed because of the absence of internal pore formation in the porous TWC particles. Conversely, porous TWC particles with interconnected pore structures were obtained when the PMMA concentration was increased to 1 and 2 wt%. This structure formed when both surface and internal pores existed in the porous TWC particles. This phenomenon occurred because the porous TWC particle surface area was not sufficiently large to accommodate all the PMMA particles on the surface, resulting in their distribution on the surface and

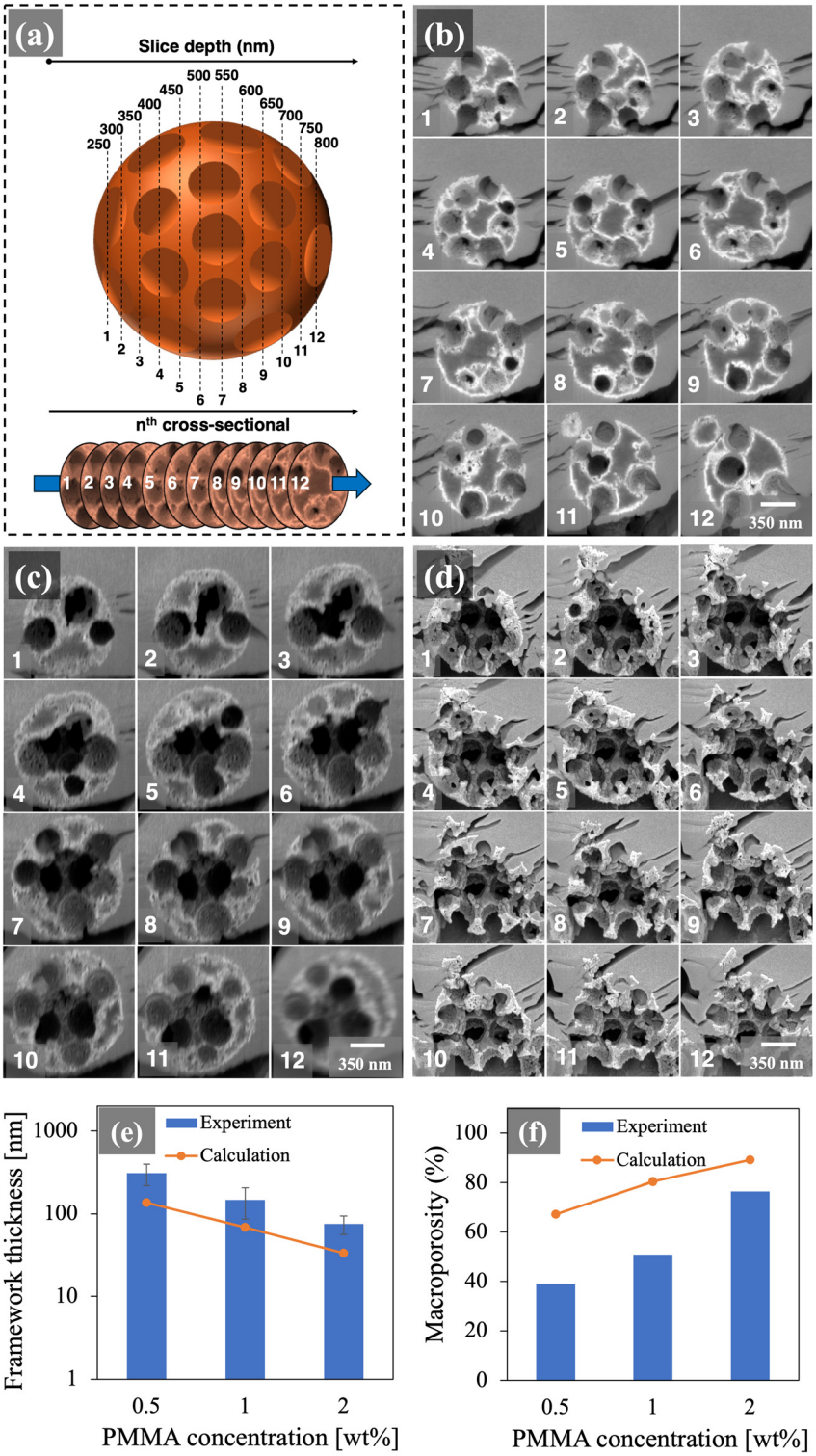

Fig. 4 (a) Schematic illustration of the cutting plane for cross-sectional observations. FIB cross-sectional SEM images of porous TWC particles prepared at PMMA concentrations of (b) 0.5, (c) 1, and (d) 2 wt% and their (e) framework thicknesses and (f) macroporosities.

in the particles. Thus, a simple numerical equation was developed to formulate the critical condition for interconnected pore structure formation in the porous TWC particles.

$$n_{\mathrm{PMMA/droplet}} \times A_{\mathrm{c\text{-}FWPMMA}} > A_{\mathrm{spc}}, \quad (2)$$

where $n_{\mathrm{PMMA/droplet}}$, $A_{\mathrm{c\text{-}FWPMMA}}$, and A_{spc} represent the number of PMMA particles in one droplet, the area of one PMMA particle including its framework thickness (Fig. S8†), and the porous TWC particle surface area, respectively. Eqn (2) shows that when the required surface area for PMMA particles on the

surface ($n_{PMMA/droplet} \times A_{c\text{-}FWPMMA}$) exceeded the porous TWC particle surface area (A_{spc}), PMMA particles were present on the surface and in the TWC particles. Conversely, when $n_{PMMA/droplet} \times A_{c\text{-}FWPMMA}$ was equal to or less than A_{spc}, all the PMMA particles could be accommodated on the surface of the particles because there was sufficient available space. Detailed information regarding the calculation of the critical point of internal pore formation is provided in section 6 of the ESI.† Fig. 5a shows the plotting curve of this equation. According to the curve, at PMMA concentrations of 0.1 and 0.5 wt%, the required surface area for PMMA particles on the surface, $n_{PMMA/droplet} \times A_{c\text{-}FWPMMA}$ (0.81 and 2.37 μm^2, respectively) was lower than their porous particle surface area, A_{spc} (1.60 and 2.68 μm^2, respectively). Thus, all the pores were accommodated on the surface of the particles. Under these conditions, no internal pore formation was observed in the porous TWC particles because of the absence of PMMA particles in the center of the particles. Thus, at PMMA concentrations of 0.1 and 0.5 wt%, no interconnected pore structure formation was observed in TP0.1 and TP0.5, consistent with the results of the particle morphology analysis. The curve showed that the critical point for interconnected pore structure formation from the calculation was at a PMMA concentration of 1.3 wt%. This result was sufficiently close to the experimental result where internal pores began to form at a PMMA concentration of 1 wt%. The difference was attributed to the less uniform pore distribution in the real porous TWC particles, resulting in internal pores forming at lower PMMA concentrations than those predicted *via* calculations. However, the total area of the PMMA particles exceeded the particle surface area at a PMMA concentration of 2 wt%. Thus, not all the PMMA particles could be accommodated on the surface of the porous particles. At this point, 41 PMMA particles were located on the surface, whereas 4 PMMA particles were in the particles (Table S3†). Thus, porous TWC particles with interconnected pore structures were obtained because of the presence of surface and internal pores. In line with this, the critical point of broken structure formation was determined. With an increase in the PMMA concentration, more TWC NPs were needed to form adequate frameworks around the PMMA particles. Thus, the minimum number of TWC NPs required for PMMA concentrations ranging from 0.1 to 3 wt% was calculated and compared with the provided TWC NPs at a TWC concentration of 1 wt%. Detailed information regarding the calculation process is provided in section 7 of the ESI.† According to the curve, the minimum number of TWC NPs required increased with an increase in the PMMA concentration (Fig. 5b). The critical point for the formation of broken structures was at a PMMA concentration of 2.1 wt%.

Fig. S10† shows the interconnected pore structure formation mechanism in the porous TWC particles, enabling a deeper comprehension of the particle self-assembly behavior of the precursor components during drying and their resulting porous properties. This process began with the generation of droplets containing precursor components of TWC NPs and PMMA particles through atomization. Considering that the precursor components possessed the same positive surface charges, repulsive interactions occurred, causing them to move individually.[37–40] As water evaporated under the heat of the vertical furnace, the droplet shrank, causing the particles to compact into composite particles.[41–46] At a low PMMA concentration of 0.5 wt%, a few PMMA particles, a large surface area, and many spaces were observed in the droplet (Fig. S10a†). This condition allowed all the PMMA particles to be accommodated on the surface composite particles. After the template removal process, porous particles with no interconnected pore structure, a thick framework, and low macroporosity were formed in the TP0.5 samples. At a concentration of 1 wt%, a moderate number of PMMA particles were present. This condition resulted in their distribution on the surface and in the composite particles because their surface area was not sufficiently large to accommodate all the PMMA particles

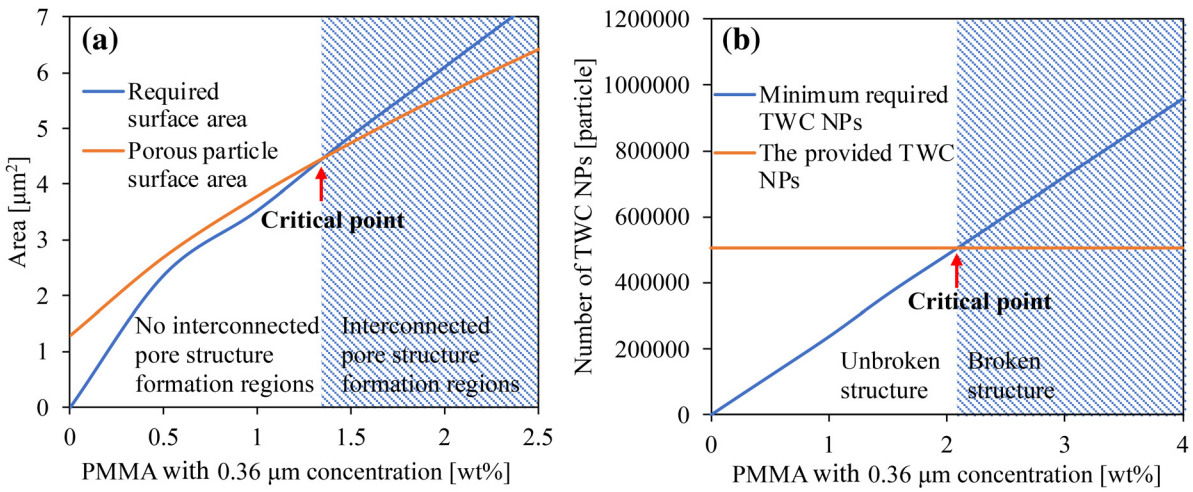

Fig. 5 Critical condition curves for the formation of (a) internal pores and (b) broken structures of porous TWC particles as the effect of PMMA concentrations.

on the surface (Fig. S10b†). This arrangement led to the formation of interconnected pores, as well as moderate framework thickness and macroporosity in the TP1 samples. Furthermore, increasing the PMMA concentration to 2 wt% resulted in a large number of PMMA particles in the droplet (Fig. S10c†). Under this condition, there was not much space in the droplet, and the particle surface area was not sufficiently large to accommodate all the PMMA particles on the surface.

Thus, TP2 exhibited unique structural morphologies, including interconnected pores, a thin framework, and high macroporosity, obtained after removing the PMMA template.

Porous TWC particles obtained at various PMMA concentrations were subjected to CO oxidation tests to evaluate their catalytic performance. Fig. 6a shows that at low temperatures from 50 °C to 110 °C, all the samples had similar CO oxidation performances. This indicated that at such low temperatures, the reaction rate was solely controlled by the inherent reactivity of the catalyst, which originated from the same physical catalytic properties. The characterization of the crystal structure, N_2 adsorption–desorption isotherms, pore-size distributions, and SSA of the selected samples (porous TWC particles with PMMA concentrations of 0.5, 1, and 2 wt%) indicated that the samples had similar physical properties (section 9, ESI†). Thus, the different structural morphologies of the porous TWC particles did not significantly contribute to the catalytic performance at low temperatures, resulting in similar catalytic performances.[13] Interestingly, within the temperature range of 120 °C–300 °C, significant differences in the CO oxidation performance were observed. According to the curve, porous TWC particles with PMMA concentrations of 0.1, 0.5, 1, and 2 wt% achieved 100% CO oxidation at 290 °C, 210 °C, 160 °C, and 130 °C, respectively. This indicated that within the aforementioned temperature range, the catalytic performance was primarily controlled by the different diffusion efficiencies of the gaseous reactants in the porous TWC particles because of their different internal structures. TP0.1 and TP0.5 required higher temperatures to achieve 100% CO oxidation compared with TP1 and TP2, suggesting a lower efficiency in the diffusion of the gaseous reactants. These phenomena were attributed to the absence of an interconnected pore structure in TP0.1 and TP0.5. According to the morphological analysis, these samples only possessed surface pores. Consequently, it was difficult for the gaseous reactants to access the active sites in the porous TWC particles. Thus, the reactants mainly interacted with the active sites around the surface pores. Conversely, the higher catalytic performance of TP1 and TP2 corresponded to the

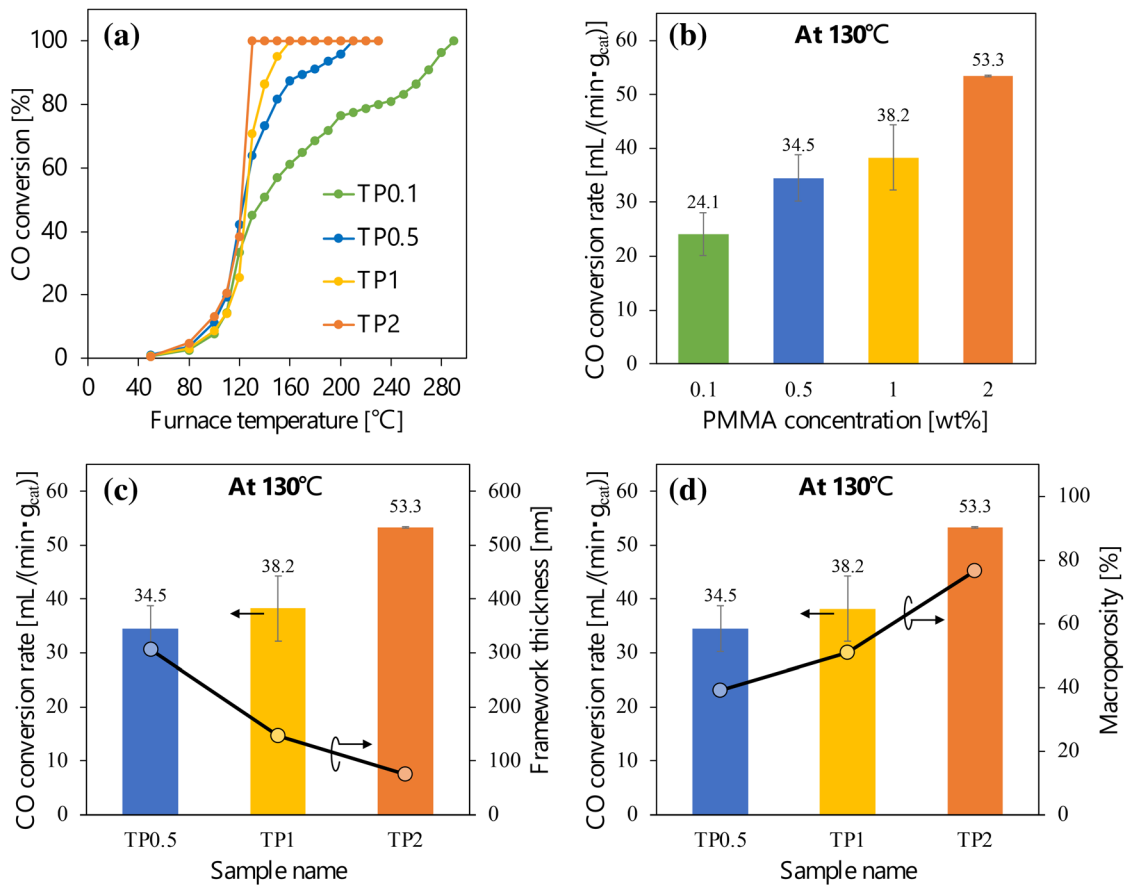

Fig. 6 (a) CO conversion into CO_2 and (b) CO oxidation rate of porous TWC particles at different PMMA concentrations and its relationship with the (c) framework thickness and (d) macroporosity at 130 °C.

interconnected pore structure formation in these samples. The continuous network extending from the surface to the interior of the porous TWC particles, provided by the interconnected pore structure, allowed gaseous reactants to access more active sites on the surface and in the internal pores. However, the more extensive interconnected pore structure observed in TP2 enhanced the convective diffusion of gaseous reactants in the TP2 particles, resulting in their superior catalytic performance compared with that of TP1. Furthermore, the CO oxidation rates of the porous TWC particle samples at 130 °C were investigated to compare the effective utilization of their internal parts (Fig. 6b). Among the other samples, the TP2 sample exhibited the highest CO oxidation rate (53.3 mL (min g_{cat})$^{-1}$). The catalytic performance of TP2 was twice that of TP0.1. This result showed an improvement in the catalytic performance of the porous TWC particles, facilitated by the effective diffusion of gaseous reactants. To better understand the improvement in the diffusion of gaseous reactants, the correlation among framework thickness, macroporosity, and the rate of CO oxidation was determined. Fig. 6c shows that the CO oxidation rate increased with a decrease in the framework thickness of the porous TWC particles. Porous TWC particles with a thin framework create lower limitations for gaseous reactants to diffuse into the framework. This condition promotes a high molecular diffusion of the gaseous reactants and effectively utilizes the internal parts within the frameworks of the porous TWC particles. Furthermore, the CO oxidation performance increased with an enhancement in the particle macroporosity (Fig. 6d). Porous TWC particles with high macroporosity can enhance the convective diffusion of gaseous reactants in the pores. Higher macroporosity indicates that macropores are more extensively distributed on the surface and internal part of porous TWC particles. These macropores provide large channels that reduce diffusion barriers and enable gaseous reactants to access the active sites more efficiently within the porous structure. Compared to catalysts with lower macroporosity, where reactants encounter more resistance and restricted access to active sites, the presence of larger macropores facilitates a greater volume of accessible channels, which can reduce diffusion resistance. Thus, porous TWC particles from a PMMA concentration of 2 wt%, with an interconnected pore structure, the thinnest framework, and the highest macroporosity, demonstrated a higher CO oxidation performance than the other samples. Following its impressive catalytic performance, this sample was further evaluated to investigate its long-term stability structure under catalytic operating conditions. Details of this investigation are provided in section 10 of the ESI.† The results demonstrate that porous TWC particles exhibited excellent stability of the porous structure, as indicated by the absence of morphological changes, such as framework collapse, pore coalescence, or structural degradation, even after a 6 h test at 130 °C. With characteristics that demonstrate high catalytic performance and structural stability over long-term usage, these particles offer great potential for use in catalytic converters for vehicle emission control. By evenly distributing the particles on the wall of the ceramic monolith in the catalytic converters, the porous TWC particles promote efficient contact with gaseous reactants. Moreover, the porous structure provides effective diffusion of gaseous reactants, leading to improved utilization of the internal part of the catalyst and enhancing catalytic performance.

Conclusions

Porous TWC particles with a precisely controlled interconnected pore structure, thin framework, and high macroporosity were fabricated using a template-assisted spray method. By adjusting PMMA concentrations (0.1–2 wt%) during the spray process, the internal pore generation was effectively controlled, forming a continuous interconnected pore network that facilitated access to active sites. Through comprehensive experimental observations and theoretical modeling, the pore structure, framework thickness, and macroporosity of the porous TWC particles were successfully predicted. FIB cross-sectional SEM images show that at a low PMMA concentration (0.5 wt%), the porous TWC particles only exhibited surface pores with several connected pores. At an optimal PMMA concentration of 2 wt%, the particles exhibited a thin framework and high macroporosity, which enhanced both molecular and convective diffusion of gaseous reactants, thereby improving the effective utilization of the internal structure. These findings highlight the importance of precisely controlled pore structures in improving mass transfer and catalytic efficiency in TWC particles, offering valuable insights for catalyst design.

Author contributions

Duhaul Biqal Kautsar: conceptualization, formal analysis, writing – original draft, and writing – review & editing; Phong Hoai Le: conceptualization, formal analysis, and writing – review & editing; Ai Ando: investigation; Eishi Tanabe: investigation; Kiet Le Anh Cao: writing – review & editing; Eka Lutfi Septiani: writing – review & editing; Tomoyuki Hirano: writing – review & editing; Takashi Ogi: conceptualization, visualization, funding acquisition, supervision, and writing – review & editing.

Data availability

The authors confirm that the data supporting the findings of this study are available within the article and its ESI.†

Conflicts of interest

There are no conflicts to declare.

Acknowledgements

This research was supported by JSPS KAKENHI Grant Numbers JP23H01745, JP22K20482, JP23K13590, and JP23KF0054. This work was also supported by JST, the establishment of university fellowships toward the creation of science and technology innovation, grant no. JPMJFS2129. This work is currently supported by a project, JPNP14004, commissioned by the New Energy and Industrial Technology Development Organization (NEDO) and the Research Association of Automotive Internal Combustion Engines. This work is partly supported by the International Network on Polyoxometalate Science at Hiroshima University, the JSPS Core-to-Core Program, and the Information Center of Particle Technology, Japan.

References

1 H. Liu, C. Cao, J. Huang, Z. Chen, G. Chen and Y. Lai, *Nanoscale*, 2020, **12**, 437–453.
2 Y. Zhang, Q. Niu, X. Gu, N. Yang and G. Zhao, *Nanoscale*, 2019, **11**, 11992–12014.
3 P. Yan, F. Ji, W. Zhang, Z. Mo, J. Qian, L. Zhu and L. Xu, *J. Colloid Interface Sci.*, 2023, **634**, 1005–1013.
4 Z. Zhang, Y. Li, X. Zhang, H. Zhang and L. Wang, *Fuel Process. Technol.*, 2021, **220**, 106892.
5 C. Huang, W. Shan, Z. Lian, Y. Zhang and H. He, *Catal. Sci. Technol.*, 2020, **10**, 6407–6419.
6 X. Jiang, J. Fan, S. Xiang, J. Mou, P. Yao, Y. Jiao, J. Wang and Y. Chen, *Appl. Surf. Sci.*, 2022, **578**, 151915.
7 L. Zhang, G. Spezzati, V. Muravev, M. A. Verheijen, B. Zijlstra, I. A. W. Filot, Y.-Q. Su, M.-W. Chang and E. J. M. Hensen, *ACS Catal.*, 2021, **11**, 5614–5627.
8 G. Spezzati, Y. Su, J. P. Hofmann, A. D. Benavidez, A. T. DeLaRiva, J. McCabe, A. K. Datye and E. J. M. Hensen, *ACS Catal.*, 2017, **7**, 6887–6891.
9 S. Sun, C. Jin, W. He, G. Li, H. Zhu and J. Huang, *J. Environ. Manage.*, 2022, **305**, 114383.
10 Y. Renème, F. Dhainaut, Y. Schuurman, C. Mirodatos and P. Granger, *Appl. Catal., B*, 2014, **160–161**, 390–399.
11 A. C. Meng, K.-B. Low, A. C. Foucher, Y. Li, I. Petrovic and E. A. Stach, *Nanoscale*, 2021, **13**, 11427–11438.
12 S. Moxon, A. R. Symington, J. S. Tse, J. M. Flitcroft, J. M. Skelton, L. J. Gillie, D. J. Cooke, S. C. Parker and M. Molinari, *Nanoscale*, 2024, **16**, 11232–11249.
13 P. H. Le, Y. Kitamoto, S. Yamashita, K. L. A. Cao, T. Hirano, T. W. M. Amen, N. Tsunoji and T. Ogi, *ACS Appl. Mater. Interfaces*, 2023, **15**, 54073–54084.
14 P. H. Le, Y. Kitamoto, K. L. A. Cao, T. Hirano, E. Tanabe and T. Ogi, *Adv. Powder Technol.*, 2022, **33**, 103581.
15 A. Zhang, G. Zhu, M. Zhai, S. Zhao, L. Zhu, D. Ye, Y. Xiang, T. Tian and H. Tang, *J. Colloid Interface Sci.*, 2023, **638**, 184–192.
16 K. Cao, X. Dai, Z. Wu and X. Weng, *Chin. Chem. Lett.*, 2021, **32**, 1206–1209.
17 X. Wang, T. Liu, H. Li, C. Han, P. Su, N. Ta, S. P. Jiang, B. Kong, J. Liu and Z. Huang, *Nano Lett.*, 2023, **23**, 4699–4707.
18 T. A. M. Suter, K. Smith, J. Hack, L. Rasha, Z. Rana, G. M. A. Angel, P. R. Shearing, T. S. Miller and D. J. L. Brett, *Adv. Energy Mater.*, 2021, **11**, 2101025.
19 H. Matsumoto, T. Iwai, M. Sawamura and Y. Miura, *ChemPlusChem*, 2024, **89**, e202400039.
20 S. Liu, X. He, X. Hu, Y. Pu and X. Mao, *Mater. Adv.*, 2024, **5**, 453–474.
21 M. Moghaddam, A. Abbassi, J. Ghazanfarian and S. Jalilian, *Chem. Eng. J.*, 2020, **388**, 124261.
22 A. A. Jones and C. D. Snow, *Chem. Commun.*, 2024, **60**, 5790–5803.
23 T. T. Nguyen, M. Miyauchi, A. M. Rahmatika, K. L. A. Cao, E. Tanabe and T. Ogi, *ACS Appl. Mater. Interfaces*, 2022, **14**, 14435–14446.
24 T. T. Nguyen, Y. Toyoda, N. S. N. Saipul Bahri, A. M. Rahmatika, K. L. A. Cao, T. Hirano, K. Takahashi, Y. Goi, Y. Morita, M. Watanabe and T. Ogi, *J. Colloid Interface Sci.*, 2023, **630**, 134–143.
25 A. M. Rahmatika, Y. Goi, T. Kitamura, W. Widiyastuti and T. Ogi, *Mater. Sci. Eng., C*, 2019, **105**, 110033.
26 A. M. Rahmatika, Y. Goi, T. Kitamura, Y. Morita, F. Iskandar and T. Ogi, *Adv. Powder Technol.*, 2020, **31**, 2932–2941.
27 D. Ren, J. Xu, S. Su, G. Tian, X. Chen, A. Zhang and C. Ai, *Constr. Build. Mater.*, 2023, **400**, 132751.
28 P.-W. Chung, A. Charmot, T. Click, Y. Lin, Y. Bae, J.-W. Chu and A. Katz, *Langmuir*, 2015, **31**, 7288–7295.
29 P. H. Le, K. L. A. Cao, Y. Kitamoto, T. Hirano and T. Ogi, *Langmuir*, 2023, **39**, 7783–7792.
30 P. H. Le, S. Yamashita, K. L. A. Cao, T. Hirano, N. Tsunoji, D. B. Kautsar and T. Ogi, *ACS Appl. Nano Mater.*, 2023, **6**, 17324–17335.
31 Y. Lin, C. Yang, Z. Wan and T. Qiu, *Int. J. Heat Mass Transfer*, 2019, **138**, 1014–1028.
32 Y. Qi, J. Zhang, L. Zhang, X. Zhou, W. Li, J. Cui, M. Fan, Y. Jin, J. Tang, J. Shen and B. Shao, *Chem. Eng. J.*, 2023, **454**, 140319.
33 C. Ferroni, M. Bracconi, M. Ambrosetti, M. Maestri, G. Groppi and E. Tronconi, *Ind. Eng. Chem. Res.*, 2021, **60**, 10522–10538.
34 C. Grove and D. A. Jerram, *Comput. Geosci.*, 2011, **37**, 1850–1859.
35 X. Shi, D. Misch and S. Vranjes-Wessely, *Gas Sci. Eng.*, 2023, **115**, 205022.
36 E. L. Septiani, S. Yamashita, D. Ratnasari, K. L. A. Cao, T. Hirano, N. Okuda, H. Matsumoto, W. Widiyastuti and T. Ogi, *Chem. Eng. Sci.*, 2024, **288**, 119820.
37 D. B. Kautsar, P. H. Le, A. Ando, K. L. A. Cao, E. L. Septiani, T. Hirano and T. Ogi, *Langmuir*, 2024, **40**, 8260–8270.
38 A. B. D. Nandiyanto, T. Ogi, W.-N. Wang, L. Gradon and K. Okuyama, *Adv. Powder Technol.*, 2019, **30**, 2908–2924.
39 T. Ogi, A. B. D. Nandiyanto and K. Okuyama, *Adv. Powder Technol.*, 2014, **25**, 3–17.

40 Z. Zhu, L. Bao, D. Pestov, P. Xu and W.-N. Wang, *Chem. Eng. J.*, 2023, **453**, 139956.
41 P. A. Kralchevsky and N. D. Denkov, *Curr. Opin. Colloid Interface Sci.*, 2001, **6**, 383–401.
42 A. F. Arif, Y. Chikuchi, R. Balgis, T. Ogi and K. Okuyama, *RSC Adv.*, 2016, **6**, 83421–83428.
43 K. L. A. Cao, F. Iskandar, E. Tanabe and T. Ogi, *KONA Powder Part. J.*, 2023, **40**, 197–218.
44 S. Wintzheimer, L. Luthardt, K. L. A. Cao, I. Imaz, D. Maspoch, T. Ogi, A. Bück, D. P. Debecker, M. Faustini and K. Mandel, *Adv. Mater.*, 2023, **35**, 2306648.
45 D. Senthil Raja and D.-H. Tsai, *Chem. Commun.*, 2024, **60**, 8497–8515.
46 K. L. A. Cao and T. Ogi, *Energy Storage Mater.*, 2025, **74**, 103901.